Visualization of a nonlinear conducting path in an organic molecular ferroelectric by using emission of terahertz radiation

M. Sotome, N. Kida, Y. Kinoshita, H. Yamakawa, T. Miyamoto, H. Mori, and H. Okamoto

Phys. Rev. B **95**, 241102 — Published 5 June 2017

DOI: 10.1103/PhysRevB.95.241102

Visualization of a nonlinear conducting path in an organic molecular ferroelectric by using emission of terahertz radiation

M. Sotome[1], N. Kida[1,2,*], Y. Kinoshita[1], H. Yamakawa[1], T. Miyamoto[1,2], H. Mori[3], and H. Okamoto[1,2]

[1]*Department of Advanced Materials Science, The University of Tokyo, 5-1-5 Kashiwa-no-ha, Chiba 277-8561, Japan*

[2]*AIST-UTokyo Advanced Operando-Measurement Technology Open Innovation Laboratory (OPERANDO-OIL), National Institute of Advanced Industrial Science and Technology (AIST), Chiba 277-8568, Japan*

[3]*The Institute for Solid State Physics, The University of Tokyo, Kashiwa, Chiba 277-8581, Japan*

* kida@k.u-tokyo.ac.jp

Abstract:

A nonlinear electric transport and switching to a negative resistance state is one of typical electric-field-induced phenomena in correlated electron materials, while their mechanisms are generally difficult to solve. In the present study, we apply the terahertz-radiation imaging method to an organic ferroelectric, α-(BEDT-TTF)$_2$I$_3$ [BEDT-TTF: bis(ethylenedithio)tetrathiafulvalene] and investigate the nature of its negative resistance phenomenon. When the negative resistance state is produced, the ferroelectric order is melted in an elongated region with the width of ~100 μm and that region grows along the direction inclined by about 40° from the *b* axis with the increase of nonlinear current. A comparison of the terahertz radiation intensity with the current magnitude revealed that the melted region forms a conducting path. We interpreted the diagonal growth of the conduction path by taking into account the anisotropy of the intermolecular transfer integrals.

PACS 78.30.Jw, 77.80.-e, 42.30.-d, 42.65.Re

Nonlinear electric transports and resistive switching phenomena are attracting considerable attention from the viewpoint not only of the non-equilibrium physics in condensed matter [1] but also of the possible mechanism for the resistance memory devices [2,3]. In correlated electron insulators, localized charge carriers can be driven by a strong electric field or current. It sometimes results in a switching from a high-resistive state to a low-resistive one accompanied by a negative differential resistance (NDR) behavior. Such a resistive switching with NDR is indeed observed in various kinds of inorganic and organic compounds, e.g., $K_{0.3}MoO_3$ [4], $Pr_{0.7}Ca_{0.3}MnO_3$ [5], $(Sr,Ca)CuO_3$ [6], $(La,Sr)_2NiO_4$ [7], potassium-7,7,8-tetracyanoquinodimethane [8], and θ-type (bis(ethylenedithio)tetrathiafulvalene)$_2$CsCo(SCN)$_4$ [9]. In most cases, however, it is difficult to obtain information related directly to the switching mechanism such as spatial images and net conductivities of conducting paths, so that mechanisms of the NDRs have not been fully understood.

To overcome this problem in NDR phenomena, in the present study, we select an α-type bis(ethylenedithio)tetrathiafulvalene (BEDT-TTF) iodide salt [α-(BEDT-TTF)$_2$I$_3$] as a target material. This compound is known to exhibit current-driven NDR [10-14] in the charge-order phase below T_{CO}=135 K. So far, several models have been proposed to explain that, such as the sliding of the charge order [10,11], the percolation of conductive ferroelectric domain walls [12], thermally excited carriers [13], and the inhomogeneous formation of conducting domains [14]. However, a conclusive interpretation has not been obtained as yet. The unique feature of this compound is that the charge order is accompanied with ferroelectricity, so that a microscopic polarization magnitude should reflect sensitively melting of the charge order. Considering this feature, we apply the terahertz-radiation imaging method [21,22,24-26] to single crystals

of α-(BEDT-TTF)$_2$I$_3$ to detect the real-space ferroelectric domain structures. By the simultaneous measurements of the terahertz radiation images and the NDR properties, we reveal that in the NDR state, the ferroelectric polarization disappears in the elongated region, which behaves as a conducting path. We discuss the growth process of the conducting path by taking into account the anisotropy of the intermolecular transfer integrals.

Figure 1(a) shows the crystal structure of α-(BEDT-TTF)$_2$I$_3$, the crystal system of which is triclinic. It consists of conducting BEDT-TTF layers and insulating I_3 layers. At room temperature, the valence of each BEDT-TTF molecule is +0.5 [Fig. 1(b)] and the quarter-filled band is formed in the BEDT-TTF layers, which is responsible for the metallic behavior. At T_{CO} =135 K, this compound undergoes a metal to charge-order-insulator transition because of the intermolecular Coulomb interactions [15] and the conductance drops by four orders of magnitudes. In the charge-order phase, BEDT-TTF molecules are classified into two types in terms of the charge-value; the charge-rich (~+0.7) molecules (A and B) and the charge-poor (~+0.3) molecules (A' and C). Each category of molecules arrange along the *b* axis in a zig-zag manner forming the horizontal stripe structure of the charge order as shown in Fig. 1(c). The space group is *P*1 and the crystal is noncentrosymmetric [16]. In addition, A and A' molecules are dimerized, so that ferroelectric polarization was expected to appear along the *a* axis [17,18]. In the charge-order phase, this compound is still a good semiconductor and the resistivity along the BEDT-TTF layers is not so high, making difficult the dielectric measurements along the layers. Thus, the dielectric properties along the layers had been unclear for a long time [9]. To obtain information about the ferroelectric polarization along the layers, the terahertz-pump optical-probe spectroscopy has recently been

applied in the charge-order phase. The results demonstrate that the direction of the ferroelectric polarization was inclined from the *b* axis by ~27°, which is parallel to the diagonal arrangement of A, B, and A' molecules [20] [Fig. 1(c)]. This study also reveals that the ferroelectricity is electronic in origin, and the macroscopic polarization is induced by the intermolecular charge transfers across the charge order transition [20]. These features in the charge-order phase are considered to be related to the NDR properties of this compound.

In the current-voltage measurements, we used the circuit with a voltage source composed of a function generator, an amplifier, and a high-voltage transformer. The experimental setup is shown in Fig. 1(d). According to the previous studies, the NDR phenomena occur commonly for the *a* and *b* directions of applied electric fields [12]. In the present study, we attach a pair of electrodes on the *ac*-surface and apply a sinusoidal voltage with a frequency of 20 Hz along the *b* axis. A road resister was inserted to prevent the sample damage by an excess current flow. The sample voltage $V_{\mathrm{s}}(t)$ and the input voltage $V_{\mathrm{in}}(t)$ were recorded by a digital oscilloscope.

For the terahertz radiation experiments, a femtosecond laser pulse delivered from a mode-locked Ti:sapphire laser (the wavelength of 800 nm, the repetition rate of 80 MHz, and the pulse width of 100 fs) was focused on the sample in the normal incidence [Figs. 1(d) and (e)]. The spot diameter *d* is ~25 μm, which corresponds to the spatial resolution. The electric field E^{ω} of the femtosecond laser pulse is parallel to the *b* axis ($E^{\omega}||b$). We detect the waveform of the terahertz-electric-field component parallel to the *b* axis (E_{THz}) by a low-temperature-grown GaAs detector. The details of the detection method was reported in Ref. 22. The phase and amplitude of E_{THz} depend on the direction and

magnitude of the ferroelectric polarization, respectively [22-25]. By using the raster scan, we can map out those values and visualize the ferroelectric domains and domain walls (DWs) [21,22,24,25]. The absorption depth of the incident *b*-axis polarized light is ~1.4 μm (=l_{d}), so that we obtain the information within ~1.4 μm from the sample surface.

In the low-temperature measurements, we use a conduction-type cryostat in which the sample is sandwiched by two 170 μm-thick glass plates with a pair of gold lines as a spacer [Fig. 1(e)]. In this method, we can cool down the sample without adhesive agent and, therefore, exclude any additional stresses on the sample, which might affect the NDR phenomena as well as the ferroelectric-domain dynamics. The sample is cooled with a rate of 0.03 K/min. Simultaneous measurements of the terahertz radiation imaging and the nonlinear electric transport are performed on a 40 μm-thick *c*-axis-oriented single crystal at 30 K.

First, we discuss the current(I_{s})–voltage(V_{s}) characteristics of the sample. Figures 2(a) shows the time profiles of $V_{\mathrm{s}}(t)$ in response to $V_{\mathrm{in}}(t)$ with load resistance $R_{\mathrm{L}} = 51.8\ \mathrm{k\Omega}$. We also show corresponding $I_{\mathrm{s}}(t)$–$V_{\mathrm{s}}(t)$ plot in Fig. 2(b). In the Ohmic region with the low sample voltage and current, the sample resistance measured by two-probe method is ~29 MΩ, which is two orders of magnitude higher than R_{L}, so that almost all of $V_{\mathrm{in}}(t)$ is applied to the sample. At $|V_{\mathrm{in}}^{\mathrm{max}}|$=41.1 V, the time profile of $V_{\mathrm{s}}(t)$ is almost the same as that of $V_{\mathrm{in}}(t)$ [Fig. 2(a1)] and I_{s} tends to linearly increase with increasing V_{s} [Fig. 2(b)]. On the other hand, when $|V_{\mathrm{in}}^{\mathrm{max}}|$=48.2 V was applied [Fig. 2(a2)], the sample was switched from a high-resistive state to a low-resistive one. As seen in Fig. 2(a2), V_{s} drops and decreases down to 5.1 V at 12.5 ms, resulting in the

NDR behavior, which is also clearly discerned by the S-shaped characteristic $I_s(t)-V_s(t)$ in Fig. 2(b). The observed S-shaped characteristic is qualitatively the same as that reported in the previous studies on α-(BEDT-TTF)$_2$I$_3$ [12] and suggests that the NDR state is driven not by the electric field but by the current. At $|V_{in}^{max}|$=304.5 V [Fig. 2(a3)], the drop of $V_s(t)$ becomes steeper, showing the rectangular shape of V_s–t characteristic [Fig. 2(a3)] and threshold V_s decreases [Fig. 2(b)].

First, we discuss the effect of the Joule heating in current-voltage measurements. In order to estimate the sample temperature through the switching phenomena, we evaluate the sample resistance R in the Ohmic (low-V_s) region from the slope of the $I_s(t)-V_s(t)$ plot in Fig. 2(b), which is shown by the dotted line. At $|V_{in}^{max}|$=41.1 V, the evaluated R is ~1 MΩ, which is an order of magnitude smaller than the R value (~29 MΩ) measured by two-probe method in the low current limit. When NDR occurs, the R value decreases; ~0.1 MΩ for $|V_{in}^{max}|$=48.2 V and ~0.05 MΩ for $|V_{in}^{max}|$=98.4 V, which are further decreased from the R value ~1 MΩ for $|V_{in}^{max}|$=41.1 V. These decreases in R observed even in the Ohmic region are attributable to the heating effect. By comparing the R values with the temperature dependence of R measured by two-probe method in the low current limit, the sample temperature is estimated to be ~61 K at $|V_{in}^{max}|$=48.2 V and ~76 K at $|V_{in}^{max}|$=304.5 V. The estimated sample temperatures are still much smaller than T_{CO}. In addition, as discussed later, the temperature dependence of the terahertz electric-field amplitude emitted from the sample is small in the CO phase (see Fig. S1 in the Supplementary Material [27]). Therefore, we can consider that the Joule heating does not play an important role on the present NDR phenomena.

When a femtosecond laser pulse is incident to an as-grown single crystal at 30 K, a

terahertz radiation with the electric-field waveform $E_{\mathrm{THz}}(t)$ shown in Fig. 3(a) is observed. The waveform shows a temporal oscillation. The terahertz wave is observed only below T_{CO}; with the decrease of temperature, its amplitude sharply increases from T_{CO} to 100 K and is almost constant below 100 K (Fig. S1 in the Supplementary Material [27]). This indicates that the emission of the terahertz wave originates from the ferroelectric polarization modulation. Figure 3(c1) shows the terahertz radiation image of the same crystal, which is the contour map of the terahertz electric-field amplitudes at 0 ps [$E_{\mathrm{THz}}(0)$]. The amplitude and sign of $E_{\mathrm{THz}}(0)$ correspond to the magnitude and direction of the ferroelectric polarization, respectively. The measured region is indicated by the dotted line in the optical microscopy image in Fig. 3(b). The terahertz radiation image in Fig. 3(c1) is homogeneous, demonstrating the formation of a single ferroelectric domain. The sample dependence and the re-cooling effects of the ferroelectric domain structures are reported in the Supplementary Material S2 [27].

Next, we discuss the terahertz radiation images in various V_{in}. At $|V_{\mathrm{in}}^{\mathrm{max}}| = 41.1\,\mathrm{V}$, the image is unchanged, still showing the single-domain structure [Fig. 3(c2)]. When the NDR occurs at $|V_{\mathrm{in}}^{\mathrm{max}}| = 48.2\,\mathrm{V}$ [Fig. 3(c3)], the terahertz radiation in the region shown in white (the upper part of the crystal) is weakened; the terahertz electric-field amplitude decreases by about 80% of the original one. It is reasonable to consider that in this region, the ferroelectric polarization and the charge order almost disappear and therefore the low-resistance state is formed. This point will be discussed later again. The width of that region is about 100 μm and its growth direction is inclined to the *b* axis by about ~40°. When $|V_{\mathrm{in}}^{\mathrm{max}}|$ is increased up to $148.1\,\mathrm{V}$, the size, the width, and the shape of the white region do not dramatically change, however, both edges of the region seem to reach the electrodes, forming a macroscopic conducting path [Fig. 3(c5)]. With

the further increase of $|V_{\mathrm{in}}^{\mathrm{max}}|$, the path grows in size, as seen in the image at $|V_{\mathrm{in}}^{\mathrm{max}}|$=393.4 V [Fig. 3(c7)]. When $|V_{\mathrm{in}}^{\mathrm{max}}|$ was decreased to zero, the image [Fig. 3(c8)] completely returned to the original one [Fig. 3(c1)].

To obtain the terahertz radiation images under larger current flows, we performed similar measurements using the road resister with the lower resistance of R_{L}=25.0 kΩ, the results of which are shown in Fig. 3(d); from (d1) to (d5), the white region, that is, the conducting path grows in the same manner as in the case of R_{L}=51.8 kΩ. When the applied voltage is further increased, the ferroelectric state is melted in the large region with the size of ~200×500 μm, as seen in Figs. 3(d6) and (d7). Such a wide conducting region was also detected in the current-driven NDR state in the previous Raman scattering studies [14]. When V_{in} was returned to zero, the original single-domain state was recovered again as shown in Fig. 3(d8).

It is valuable to compare quantitatively the changes in the terahertz radiation images (Fig. 3) with the nonlinear electric-transport characteristics (Fig. 2). For R_{L}= 25.0 kΩ in the terahertz radiation experiments, we integrate $E_{\mathrm{THz}}(0)$ over all the area of the crystal and plotted that value $E_{\mathrm{THz}}^{\mathrm{total}}(0)$ by circles in Fig. 4(a) as a function of $I_{\mathrm{s}}(12.5\ \mathrm{ms})$. $E_{\mathrm{THz}}^{\mathrm{total}}(0)$ decreases with increasing $I_{\mathrm{s}}(12.5\ \mathrm{ms})$. We also show the resistance (12.5 ms), $R(12.5\ \mathrm{ms})$, by a gray solid line, which was estimated from $I_{\mathrm{s}}(t)$–$V_{\mathrm{s}}(t)$ characteristics (Fig. 2). When the NDR occurs, $R(12.5\ \mathrm{ms})$ drops by five orders of magnitude. In order to estimate the ferroelectric high-resistive state with a volume fraction *f*, we adopt a simple parallel circuit model, in which we assume that the ferroelectric (FE) high-resistive state with *f* and non-ferroelectric (NFE) low-resistive one with a volume fraction (1-*f*) connect parallel two electrodes as illustrated in Fig. 4(b). Using this model, we evaluate *f* as $R(12.5\ \mathrm{ms}) = \left[f/R_{\mathrm{High}} + (1-f)/R_{\mathrm{Low}}\right]^{-1}$,

where R_{High} and R_{Low} are the resistance of the low- and high-resistive states, respectively. In this model, R_{High} is assumed to be 3 kΩ, which is the resistance value at 0 ms, and R_{Low} is a parameter. In Fig. 4(a), we show by a blue solid line *f* as a function of $I_{\mathrm{s}}(12.5\ \mathrm{ms})$. *f* with R_{Low}=100 Ω and $E_{\mathrm{THz}}^{\mathrm{total}}(0)$ (circles) decrease with increasing $I_{\mathrm{s}}(12.5\ \mathrm{ms})$. The agreement of $E_{\mathrm{THz}}^{\mathrm{total}}(0)$ and *f* ensures the validities of our model and parameter (R_{Low}=100 Ω); R_{Low}=100 Ω is comparable with the resistance in the metallic phase. Thus, we conclude that the NDR occurs by the formation of the macroscopic low-resistive path in which the ferroelectric polarization completely disappears and therefore the charge order is melted. The differences between *f* and $E_{\mathrm{THz}}^{\mathrm{total}}(0)$ in the NDR state are attributed probably to simple estimation of $E_{\mathrm{THz}}^{\mathrm{total}}(0)$. In our estimation, $E_{\mathrm{THz}}^{\mathrm{total}}(0)$ are temporary averaged, while *R* values are not averaged. In addition, terahertz lights are emitted not from all the crystal but only from the finite region determined by the penetration depth (~1.4 μm) of an incident femtosecond laser pulse.

Finally, we briefly discuss the direction of the macroscopic conduction path in the NDR state. As seen in Figs. 3(c) and (d), the conducting path is inclined by ~40° from the *b* axis. This inclination (~40°) is observed in several samples and is close to the direction (~27°) of the arrangement of A, B, and A' molecules [Fig. 1(c)]. In this direction, the intermolecular electron transfer integral is relatively large as compared to the other directions such as the *a* axis, the *b* axis, and the A'-B-A direction [16]. This suggests that the intermolecular charge-back transfer processes trigger the melting of the ferroelectric charge order, resulting in the formation of the conducting path.

In summary, we detected the changes of the ferroelectric state under the nonlinear

current flow in the charge-order phase of α-(BEDT-TTF)$_2$I$_3$ by using the terahertz-radiation imaging method. The increase of the voltage applied to the single crystal sample gave rise to the NDR state and then the ferroelectric order disappeared in the elongated region with the width of ~100 μm, exhibiting the formation of the macroscopic conducting path. The direction of this conducting path is inclined by about 40° from the *b*-axis, which can be interpreted by the anisotropy in the intermolecular transfer integrals.

Acknowledgements

This work was partly supported by a Grant-in-Aid by MEXT (Nos. 24340074, 25247049, 25600072, 26610096, 15H03549, 16H04010, and No. 25-3372), the Canon Foundation, and CREST, Japan Science and Technology Agency. M. S., Y. K., and H. Y. were supported by Japan Society for the Promotion of Science (JSPS) through Program for Leading Graduate Schools (MERIT). M. S., Y. K., and H. Y. were also supported by JSPS Research Fellowships for Young Scientists.

References

[1] H. Aoki, N. Tsuji, M. Eckstein, M. Kollar, T. Oka, and P. Werner, Nonequilibrium dynamical mean-field theory and its applications, Rev. Mod. Phys. **86**, 779 (2014).

[2] R. Waser, and M. Aono, Nanoionics-based resistive switching memories, Nat. Mater. **6**, 833 (2007).

[3] A. Sawa, Resistive switching in transition metal oxides, Materials Today **11**, 28 (2008).

[4] G. Grüner, The dynamics of charge-density wave, Rev. Mod. Phys. **60**, 1129 (1988).

[5] A. Asamitsu, Y. Tomioka, H. Kuwahara, and Y. Tokura, Current switching of resistive states in magnetoresistive manganites, Nature (London) **388**, 50 (1997).

[6] Y. Taguchi, T. Matsumoto, and Y. Tokura, Dielectric breakdown of one-dimensional Mott insulators $SrCuO_3$ and $CaCuO_3$, Phys. Rev. B **62**, 7015 (2000).

[7] S. Yamanouchi, Y. Taguchi, and Y. Tokura, Dielectric breakdown of the insulating charge-ordered state in $La_{2-x}Sr_xNiO_4$, Phys. Rev. Lett. **83**, 5555 (1999).

[8] R. Kumai, Y. Okimoto, and Y. Tokura, Current-induced insulator-metal transition and pattern formation in an organic charge-transfer complex, Science **284**, 1645 (1999).

[9] F. Sawano, I. Terasaki, H. Mori, T. Mori, M. Watanabe, N. Ikeda, Y. Nogami, and Y. Noda, An organic thyristor, Nature (London) **437**, 522 (2005).

[10] M. Dressel, G. Grüner, J.P. Pouget, A. Breining, and D. Schweitzer, Field and frequency dependent transport in the two-dimensional organic conductor α-$(BEDT\text{-}TTF)_2I_3$, J. Phys. I France **4**, 579 (1994).

[11] K. Tamura, T. Ozawa, Y. Bando, T. Kawamoto, and T. Mori, Voltage oscillation associated with nonlinear conductivity in the organic conductor α-$(BEDT\text{-}TTF)_2I_3$, J. Appl. Phys. **107**, 103716 (2010).

[12] T. Ivek, I. Kovačević, M. Pinterić, B. Korin-Hamzić, S. Tomic, T. Knoblauch, D. Schweitzer, and M. Dressel, Cooperative dynamics in charge-ordered states of α-$(BEDT\text{-}TTF)_2I_3$, Phys. Rev. B **86**, 245125 (2012).

[13] K. Kodama, M. Kimata, Y. Takahide, N. Kurita, A. Harada, H. Satsukawa, T.

Terashima, S. Uji, K. Yamamoto, and K. Yakushi, Charge transport in charge-ordered states of two-dimensional organic conductors, α-(BEDT-TTF)$_2$I$_3$ and α'-α-(BEDT-TTF)$_2$IBr$_2$, J. Phys. Soc. Jpn. **81**, 044703 (2012).

[14] A. Ito, Y. Nakamura, A. Nakamura, and H. Kishida, Measurements of the nonlinear conducting states of α-(BEDT-TTF)$_2$I$_3$ using electronic Raman scattering, Phys. Rev. Lett. **111**, 197801 (2013).

[15] H. Seo, C. Hotta, and H. Fukuyama, Toward systematic understanding of diversity of electronic properties in low-dimensional molecular solids, Chem. Rev. **104**, 5005 (2004).

[16] T. Kakiuchi, Y. Wakabayashi, H. Sawa, T. Takahashi, and T. Nakamura, Charge ordering in α-(BEDT-TTF)$_2$I$_3$, by synchrotron X-ray diffraction, J. Phys. Soc. Jpn. **76**, 113702 (2007).

[17] K. Yamamoto, S. Iwai, S. Boyko, A. Kashiwazaki, F. Hiramatsu, C. Okabe, N. Nishi, and K. Yakushi, Strong optical nonlinearity and its ultrafast response associated with electron ferroelectricity in an organic conductor, J. Phys. Soc. Jpn. **77**, 074709 (2008).

[18] K. Yamamoto, A. A. Kowalska, and K. Yakushi, Direct observation of ferroelectric domains created by Wigner crystallization of electrons in α-[bis(ethylenedithio)tetrathiafulvalene]$_2$I$_3$, Appl. Phys. Lett. **96**, 122901 (2010).

[19] P. Lunkenheimer, B. Hartmann, M. Lang, J. Müller, D. Schweitzer, S. Krohns, and A. Loidl, Ferroelectric properties of charge-ordered α-(BEDT-TTF)$_2$I$_3$, Phys. Rev. B **91**, 245132 (2015).

[20] H. Yamakawa, T. Miyamoto, T. Morimoto, H. Yada, Y. Kinoshita, M. Sotome, N. Kida, K. Yamamoto, K. Iwano, Y. Matsumoto, S. Watanabe, Y. Shimoi, M. Suda,

H. M. Yamamoto, H. Mori, and H. Okamoto, Novel electronic ferroelectricity in an organic charge-order insulator investigated with terahertz-pump optical-probe spectroscopy, Sci. Rep. **6**, 20571 (2016).

[21] K. Takahashi, N. Kida, and M. Tonouchi, Terahertz radiation by an ultrafast spontaneous polarization modulation of multiferroic $BiFeO_3$ thin films, Phys. Rev. Lett. **96**, 117402 (2006).

[22] M. Sotome, N. Kida, S. Horiuchi, and H. Okamoto, Visualization of ferroelectric domains in a hydrogen-bonded molecular crystal using emission of terahertz radiation, Appl. Phys. Lett. **105**, 041101 (2014).

[23] W. Guan, W, N. Kida, M. Sotome, Y. Kinoshita, R. Takeda, A. Inoue, S. Horiuchi, and H. Okamoto, Terahertz radiation by optical rectification in a hydrogen-bonded organic molecular ferroelectric crystal, 2-phenylmalondialdehyde, Jpn. J. Appl. Phys. **53**, 09PD07 (2014).

[24] M. Sotome, N. Kida, S. Horiuchi, and H. Okamoto, Terahertz radiation imaging of ferroelectric domain topology in room-temperature hydrogen-bonded supramolecular ferroelectrics, ACS Photonics **2**, 1373 (2015).

[25] Y. Kinoshita, N. Kida, M. Sotome, R. Takeda, N. Abe, M. Saito, T. Arima, and H Okamoto, Visualization of ferroelectric domains in boracite using emission of terahertz radiation, Jpn. J. Appl. Phys. **53**, 09PD08 (2014).

[26] Y. Kinoshita, N. Kida, M. Sotome, T. Miyamoto, Y. Iguchi, Y. Onose, and H. Okamoto, Terahertz radiation by subpicosecond magnetization modulation in the ferrimagnet $LiFe_5O_8$, ACS Photonics **3**, 1170 (2016).

[27] See, supplementary information for temperature dependence of the terahertz radiation and terahertz radiation imaging in a virgin state.

FIG. 1. (a) Crystal structure of α-(BEDT-TTF)$_2$I$_3$. BEDT-TTF molecules in (b) metallic and (c) charge-order insulating phases. Schematics of (d) the setup for simultaneous current-voltage and ferroelectric domain imaging using terahertz radiation measurements and (e) expanded view.

FIG. 2. (a) Time profiles of the sample voltage $V_{\mathrm{s}}(t)$ in response to the input voltage $V_{\mathrm{in}}(t)$ with R_{L}=51.8 kΩ. (b) Corresponding sample current $I_{\mathrm{s}}(t)$ as a function of $V_{\mathrm{s}}(t)$.

FIG. 3. (a) Terahertz waveform in $E^{\omega}||b$ and $E_{\mathrm{THz}}||b$, measured at 30 K. (b) Optical microscopy image of the *c*-axis-oriented single crystal. Terahertz radiation images as a function of the input voltage with (c) R_{L}=51.8 kΩ and (d) R_{L}=25.0 kΩ.

FIG. 4. (a) Resistance at 12.5 ms (a gray solid line) from current-voltage characteristics as a function of the sample current with R_{L}=25.0 kΩ. Circles represent total terahertz electric-field magnitudes, $E_{\mathrm{THz}}^{\mathrm{total}}(0)$, which were integrated over all the area of the crystal, as a function of the sample current. We also show the calculated *f* by a blue solid line. (b) Schematic of the parallel circuit model with a volume fraction *f* of the ferroelectric region.

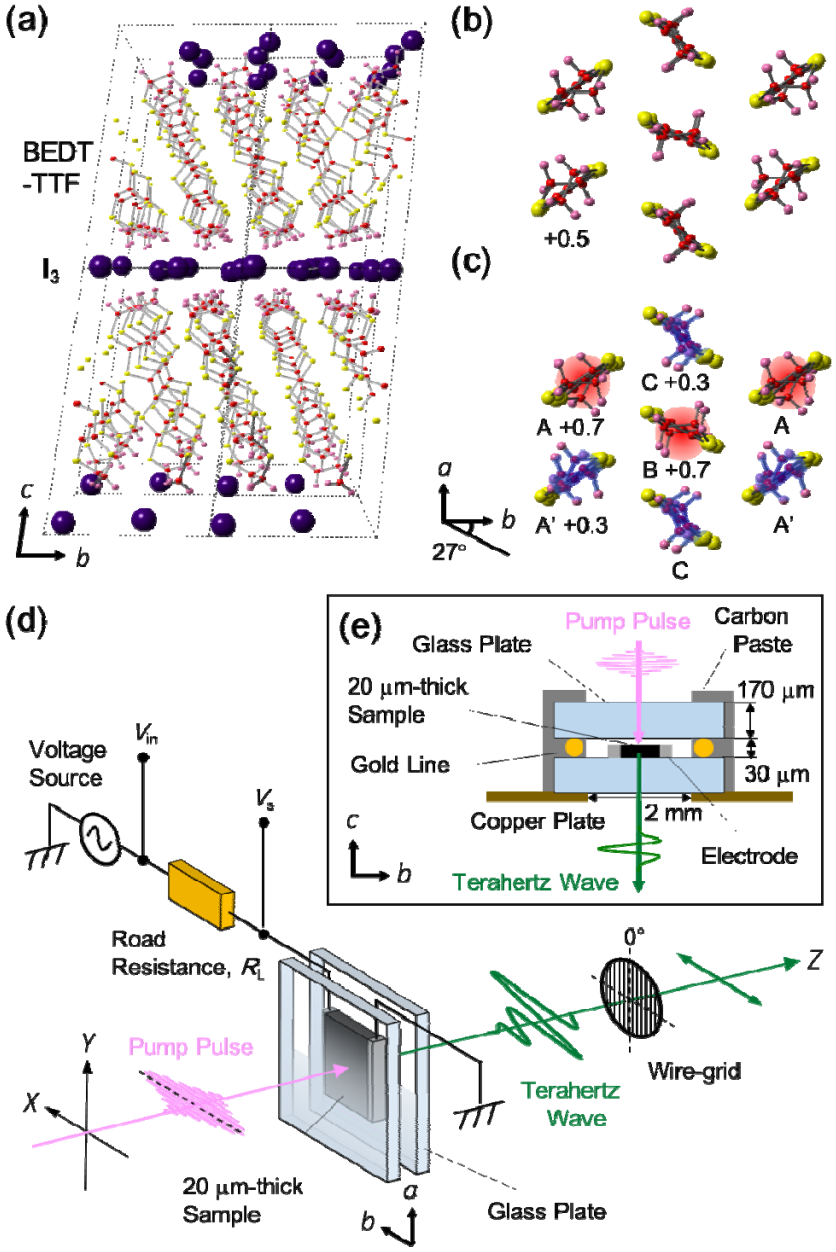
(a)
BEDT
-TTF
I_3
c
b
(b)
+0.5
(c)
C +0.3
A +0.7
A
B +0.7
A' +0.3
A'
C
a
b
27°
(d)
Voltage
Source
V_{in}
V_s
Road
Resistance, R_L
Pump Pulse
Y
X
20 μm-thick
Sample
a
b
Glass Plate
Terahertz
Wave
0°
Z
Wire-grid
(e)
Glass Plate
Pump Pulse
Carbon
Paste
20 μm-thick
Sample
170 μm
Gold Line
30 μm
2 mm
Copper Plate
Electrode
c
b
Terahertz Wave

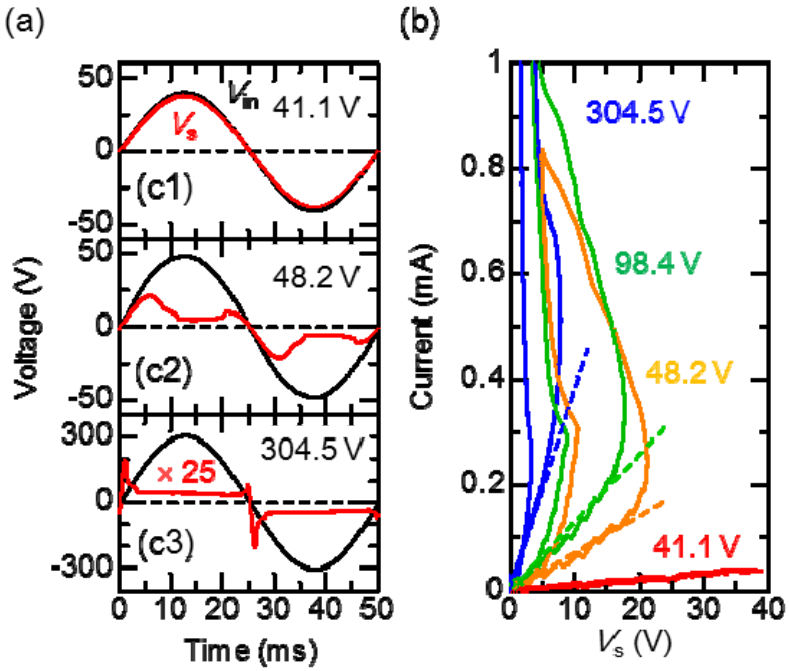
(a)
(b)
50
0
-50
V_{in} 41.1 V
V_s
(c1)
50
0
-50
48.2 V
(c2)
300
0
-300
304.5 V
× 25
(c3)
Voltage (V)
0 10 20 30 40 50
Time (ms)
1
0.8
0.6
0.4
0.2
0
Current (mA)
304.5 V
98.4 V
48.2 V
41.1 V
0 10 20 30 40
V_s (V)

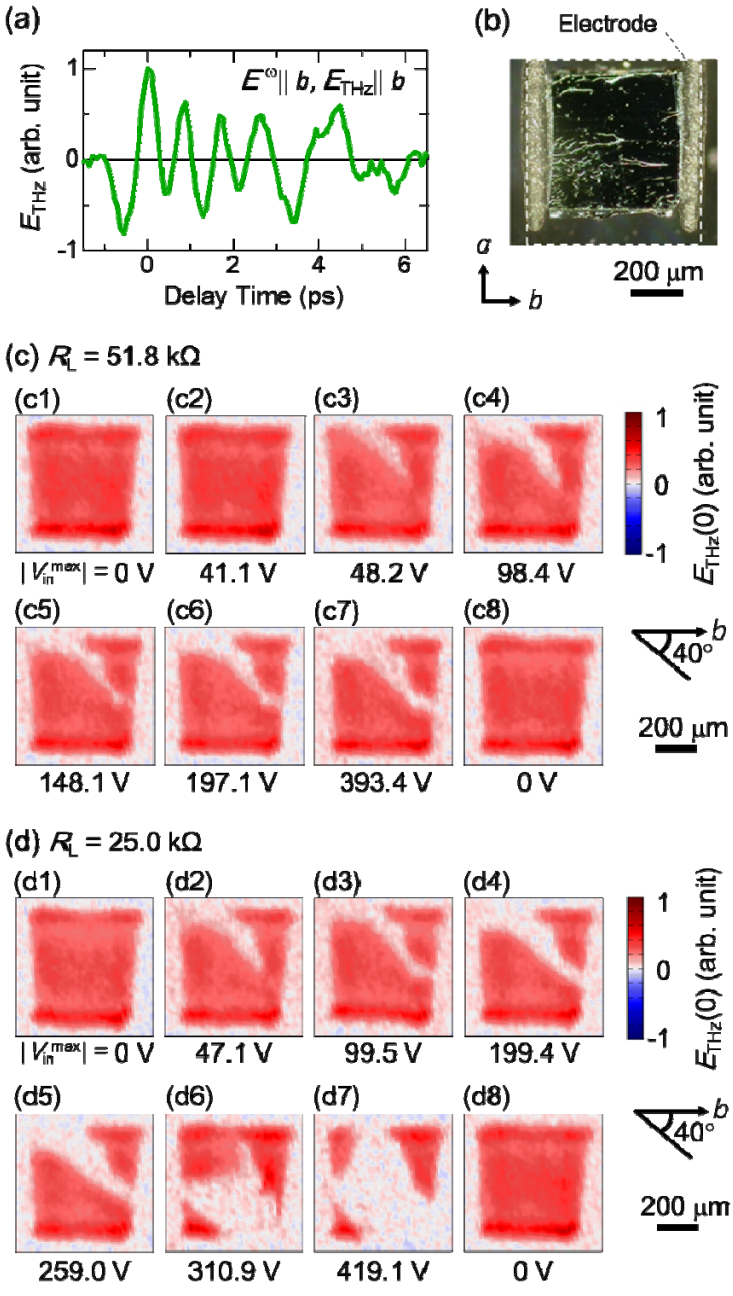
(a)
E^{ω}|| b, E_{THz}|| b
E_{THz} (arb. unit)
Delay Time (ps)
(b)
Electrode
a
b
200 μm
(c) R_L = 51.8 kΩ
(c1)
(c2)
(c3)
(c4)
$|V_{in}^{max}|$ = 0 V
41.1 V
48.2 V
98.4 V
(c5)
(c6)
(c7)
(c8)
148.1 V
197.1 V
393.4 V
0 V
E_{THz}(0) (arb. unit)
40°
200 μm
(d) R_L = 25.0 kΩ
(d1)
(d2)
(d3)
(d4)
$|V_{in}^{max}|$ = 0 V
47.1 V
99.5 V
199.4 V
(d5)
(d6)
(d7)
(d8)
259.0 V
310.9 V
419.1 V
0 V

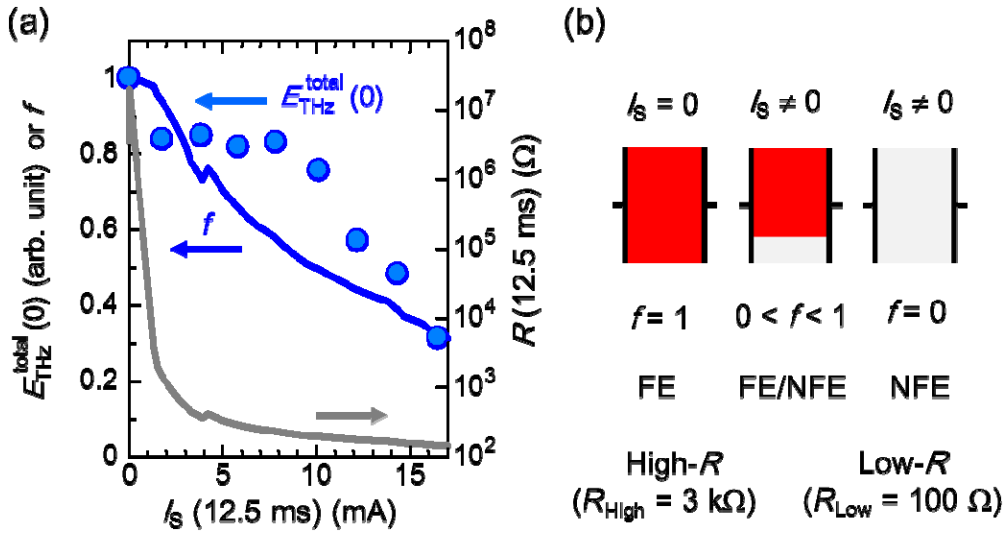
(a)
(b)
E_{THz}^{total} (0)
f
E_{THz}^{total} (0) (arb. unit) or f
R (12.5 ms) (Ω)
I_S (12.5 ms) (mA)
I_S = 0
I_S ≠ 0
I_S ≠ 0
f = 1
0 < f < 1
f = 0
FE
FE/NFE
NFE
High-R
(R_{High} = 3 kΩ)
Low-R
(R_{Low} = 100 Ω)